stellarator news

Published by Fusion Energy Division, Oak Ridge National Laboratory
Building 9201-2 P.O. Box 2009 Oak Ridge, TN 37831-8071, USA

Editor: James A. Rome Issue 77 September 2001
E-Mail: jar@ornl.gov Phone (865) 574-1306
On the Web at *http://www.ornl.gov/fed/stelnews*

Electron Bernstein emission electron temperature profile diagnostic at the W7-AS stellarator

Stellarators reach high densities and eventually exceed the accessibility limit for electromagnetic electron cyclotron (EC) waves polarized in the ordinary (O) or extraordinary (X) mode. For instance, in recent island divertor experiments at Wendelstein VII-AS (W7-AS) (R = 2.0 m, a < 0.17 m, B = 2.5 T) a stationary central density $n_e = 3.5 \times 10^{20}$ m^{-3} was reached [1]. This is almost three times the cutoff value for the common EC heating and diagnostic scenario (second harmonic X-mode, low field side).

Since 1996, electron Bernstein waves (EBWs) have been routinely employed at W7-AS for overdense plasma heating in the EC frequency range [2]. The Bernstein (B) mode, the third electron cyclotron mode in a *hot* magnetized plasma, shows the interesting characteristic of propagation without an upper density limit. On the other hand, it is an electrostatic mode, unable to propagate in vacuum, which has to be excited within the plasma. At W7-AS it is excited at the upper hybrid layer after a double (O-X-B) mode conversion, according to the scheme proposed by Preinhaelter and Kopecky in 1973 [3]. The conditions for efficient O-X and X-B conversion are, respectively, a proper oblique launch geometry, implying coalescence of O- and X-mode at the O-mode cutoff, and a not too cold plasma edge, in order to avoid collisional losses at the upper hybrid layer.

Thanks to the reverse (B–X–O) mechanism, electron Bernstein emission (EBE) can escape the plasma and reach an external antenna [4]. Since the plasma is optically thick for these waves, emission reaches blackbody levels [4] and can be used to diagnose the temperature profile of overdense plasmas with space and time resolution as good as that for electron cyclotron emission (ECE) of underdense plasmas, as we demonstrate here.

A Gaussian optic antenna consisting of an ellipsoidal mirror and a corrugated horn was installed in the W7-AS vessel (Fig.1). The sightline was optimized for EBWs and B–X–O conversion by means of ray-tracing calculations involving the hot dielectric tensor and three-dimensional (3-D) stellarator geometry. In particular, the transmittivity was maximized (in the sense of [3]), and the spectrum deformation due to the oblique nature of the sightline itself was minimized by searching for the best toroidal position ϕ.

In a stellarator, in fact, ϕ represents one more degree of freedom, affecting the evolution of the Doppler-relevant component $N_{||}$ of the EBW refractive index, which thus can be minimized by means of a toroidal scan in ray-tracing calculations.

Moreover, the antenna selects pure O-mode emission; the O-mode polarization, which is elliptical because of the oblique sightline, is linearized by a $\lambda/4$ phase shifter. The phase shift originates from the different phase velocity for orthogonal modes in an elliptical waveguide; after trying

In this issue . . .

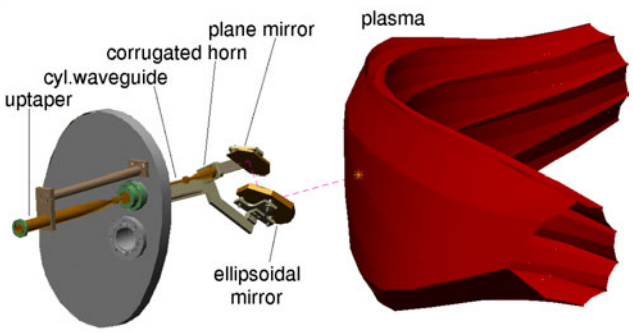

Fig. 1. In-vessel part of the diagnostic.

several devices, we found one that was broadband enough for diagnostic requirements.

The signal, now linearly polarized, is spectrum-analyzed in the 63- to 78-GHz band by the first harmonic O-mode ECE heterodyne radiometer, upgraded to 48 channels.

Figure 2 shows an EBE spectrum in a discharge heated by neutral beam injection (NBI), rescaled to take into account the fact that the transmittivity is <100%. In fact, in spite of antenna optimization for penetration through a *laminar* cutoff layer, a realistic *turbulent* layer is corrugated and oscillates, and therefore can locally and transiently form a nonoptimal angle with the ray. The effect is small and a transmittivity of 75–85% is found, thanks to the short length scale $L_n = n_e/(\partial n_e/\partial r)$ of the density profile in the gradient region. In fact, typical W7-AS values of $k_0 L_n$ = 15–60, where k_0 is the free-space wavelength, yield effective O–X coupling in a Gaussian cone of aperture 7°–16° around the best direction [3–5]. Therefore, turbulence-induced deviations from the optimal angle are negligible if they are smaller than this aperture.

The wide cone aperture offers the further advantage that, although the optimal angle depends on probe frequency and magnetic field, the adopted (fixed) sightline suits the whole frequency range of the EBE spectrum and a wide magnetic field interval, B = 2.1–2.5 T on axis.

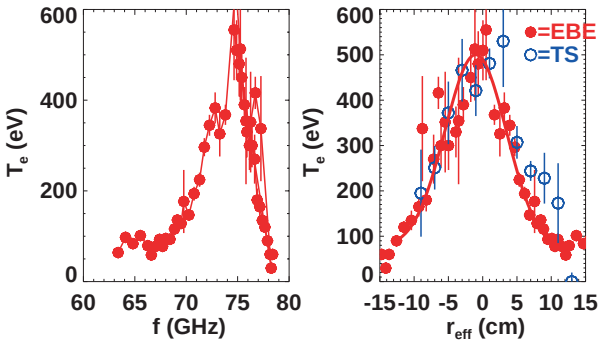

Fig. 2. EBE spectrum (left) and profile (right, closed symbols) and Thomson scattering profile (right, open symbols).

In short, the diagnostic is robust with respect to O–X conversion, even without steerable mirrors or gratings. Limitations may come only from the other conversion, whose efficiency depends on edge temperature, as already mentioned. For example, signal degradation was observed occasionally at plasma detachment and was interpreted as X–B efficiency degradation subsequent to cooling of the edge.

Conversion of EBE spectra in profiles is not as straightforward as ECE. Because of the complicated EBW ray paths, especially given the strong dependence of refractive index on magnetic topology, the shift of emitting layers with respect to the $\omega = \omega_c$ layers can be determined only after accurate ray-tracing calculations.

Experimental density data and equilibrium code magnetic data are assigned as input to the parallel version of the same ray-tracing code used for antenna optimization. This maps the channel frequencies into the corresponding emitting locations in plasma, allowing profile recovery.

Indeed, as the temperature profile is also an input for calculations that involve the *hot* dielectric tensor, a "guess" is necessary at the beginning, but in 2–4 iterations the code converges, within error bars, to the definitive profile (Fig. 2, right). Vertical error bars of about 10% are associated with the uncertainty in radiometer calibration with a hot/cold source. Horizontal error bars of 0.5–1 cm in profiles are assigned according to emission region widths computed by the ray tracing code.

The heat wave method, an important tool for energy transport investigations, has been extended for the first time to overdense plasmas combining EBW heating and diagnostic. The plasma cannot be diagnosed and heated at the same harmonic because the heating beam drives a parametric instability at the upper hybrid layer, where the X–B conversion occurs. Such instability results in high nonthermal peaks overlapping the thermal spectrum [3].

This problem was overcome by combining EBE measurements at the first harmonic (63–78 GHz) with EBW heating at the second harmonic (140 GHz), modulated in this case with a frequency of 184 Hz. The plasma had to be overdense up to the second harmonic O-mode, i.e., $n_e > 2.4 \times 10^{20} \mathrm{m}^{-3}$.

A cross-correlation analysis of the EBE channel's response to periodic temperature perturbation yields the heat wave amplitudes and phases plotted in Fig. 3. The two amplitude peaks and delay zeros correspond to off-axis power deposition at $r_{\mathrm{eff}} \cong 5$ cm. High-beta effects such as the Shafranov shift are not yet included in the analysis and are expected to remove the systematic 1.5 cm offset. Heat waves can be recognized in Fig. 3, propagating from deposition regions inward and outward.

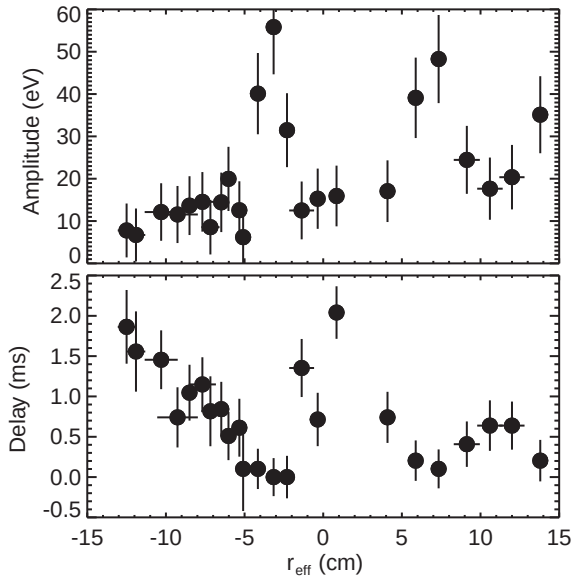

Fig. 3. Heat wave amplitude and phase for $n_e = 3 \times 10^{20}$ m^{-3}.

Innovative applications of the EBE diagnostic may concern phenomena occurring at densities too high for ECE and over time scales too short for Thomson scattering.

Examples are L/H mode transitions and edge-localized modes (ELMs), which at W7-AS often take place at densities out of the ECE operational range, $n_e > 1.2 \times 10^{20}$ m^{-3} (see Figs. 1 and 4 in Ref. [6]).

Figure 4 shows EBE measurements of ELMs at $n_e = 1.4 \times 10^{20}$ m^{-3}, with 1-μs time resolution. As expected, edge EBE is correlated with H_α, mostly coming from the edge.

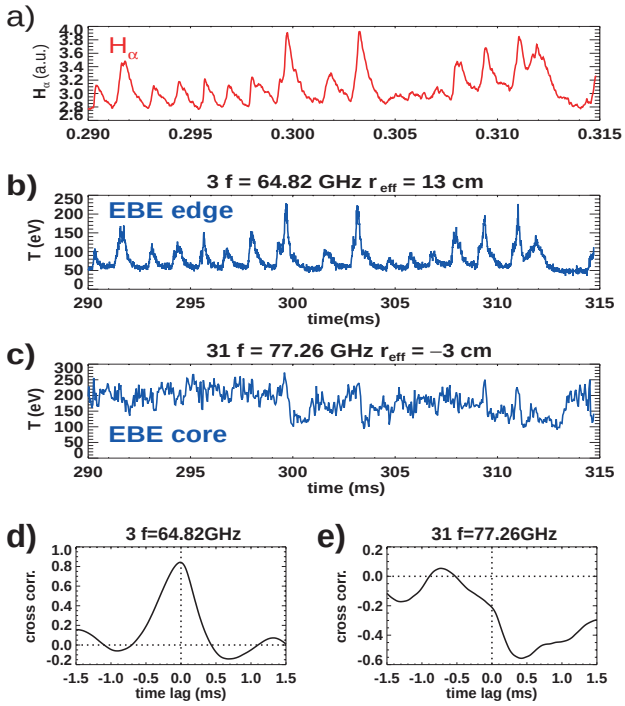

Fig. 4. ELMs measured by: a) H_α, b) edge EBE, c) core EBE. Correlations of H_α with: d) edge EBE, e) core EBE.

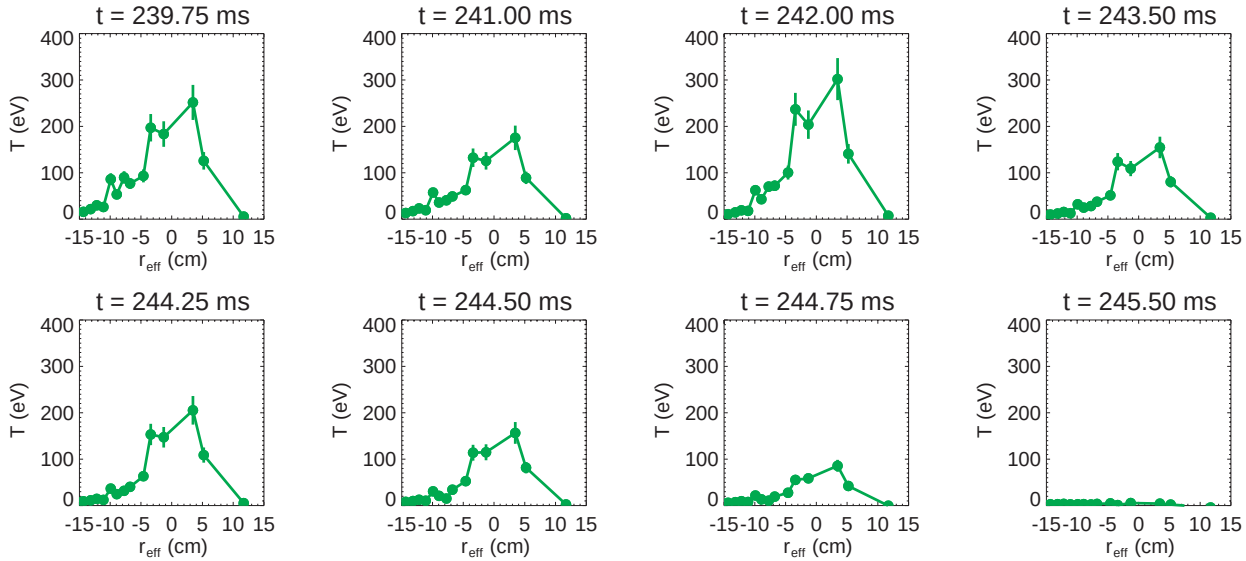

Fig. 5. Profile oscillations before radiative collapse, over a millisecond scale.

On the other hand, for any edge temperature spike, the core temperature drops. This is easily visible in correspondence with the two biggest spikes in Fig. 4 and is confirmed for the whole sample by a negative correlation with H_α. The time lag for propagation of temperature information from edge to center is 0.4 ms in the considered limiter discharge.

Another high-density fast phenomenon at W7-AS is the radiative collapse [7]. Figure 5 shows temperature profile oscillations observed by EBE before the definitive collapse. A single collapse is a transition from one stable branch to another of the multistable solution of the time-dependent temperature diffusion problem [8]. Observed oscillations can therefore be interpreted as multiple transitions between the two states, like a hysteresis cycle along the S-shaped solution.

References

(A detailed bibliography on mode-converted EBWs can be found on: http://www.ipp.mpg.de/~frv/bib.html).

[1] P. Grigull et al., to be published in Plasma Phys. Controlled Fusion, January 2002.

[2] H. P. Laqua et al., Phys. Rev. Lett. **78**, 3467 (1997) and Stellarator News 44 (1996).

[3] J. Preinhaelter and V. Kopecky, J. Plasma Phys. **10**, 1 (1973).

[4] H. P. Laqua et al., Phys. Rev. Lett. **81**, 2060 (1998).

[5] F. Volpe et al., Proc. 27th EPS Conf. Controlled Fusion and Plasma Phys., Budapest 2000, p.1669.

[6] M. Hirsch et al., Plasma Phys. Controlled Fusion **42**, A231 (2000).

[7] L. Giannone et al., Plasma Phys. Controlled Fusion **42**, 603 (2000).

[8] P. Bachmann et al., Proc. 24th EPS Conf. Controlled Fusion and Plasma Phys., Berchtesgaden 1997, p.1817.

F. Volpe, H. P. Laqua, and the W7-AS Team
Max Planck Institut für Plasmaphysik
Garching bei München, Germany

E-mail: francesco@ipp.mpg.de
Phone: 0049-89-3299-1822

First island divertor experiments on W7-AS

Wendelstein VII-AS (W7-AS) has recently been equipped with an open island divertor in order to experimentally evaluate the concept in view of future application to W7-X. The divertor consists of ten identical modules — two per field period — placed at the top and bottom of the elliptical cross sections, as shown in Fig. 1. With the exception of the dimensions, the geometry is similar to that planned for W7-X [1]. Each module is composed of an inertially cooled target made of carbon fiber composite (CFC), which intersects "natural" magnetic islands at the edge (edge rotational transform $\iota_a = 5/9$), and of baffles (isotropic graphite). The targets are three-dimensionally shaped in order to achieve nearly homogeneous thermal load distributions in the helical direction. The chambers behind the slits separating the targets and inboard baffles are equipped with titanium evaporators for gettering of neutrals (not yet applied). Most target tiles are instrumented with thermocouples; two opposite (top and bottom) modules are equipped with target-integrated, flush-mounted Langmuir probe arrays (for locations, see below). The island topological parameters relevant for flux diversion can be varied within a broad range by means of special coils controlling the $B_{5,m}$ perturbation field magnitude.

For the experiments reported, a configuration with a field line connection length of $L_c \sim 100$ m (1 cm inside the island separatrix) between stagnation plane and target and a minimum separation of $\Delta_x \sim 4$ cm between X-points and targets was found to represent a preliminary optimum. Initial efforts were focused mainly on the impact of the new divertors on the core plasma performance and on the type of divertor regimes that can be established with this geometry [2].

Plasma performance at high density

The new divertors enable access to a new NBI- heated, very high density (up to $n_e = 3.5 \times 10^{20}$ m^{-3}) operating regime with promising confinement properties, which we designate the Ultra High Density (UHD) regime. Former high-power NBI discharges with limiters were generally transient in W7-AS. Within the accessible density range of up to about 2×10^{20} m^{-3}, the particle and impurity confinement times were rather long and increased with density. The density could not be controlled, and often both the density and the radiation from the core quickly increased until the discharges collapsed. The density at the upstream separatrix position n_{es} increased less than linearly with the line-averaged density, and n_{es} values high enough for favorable divertor regimes could be achieved only transiently [3].

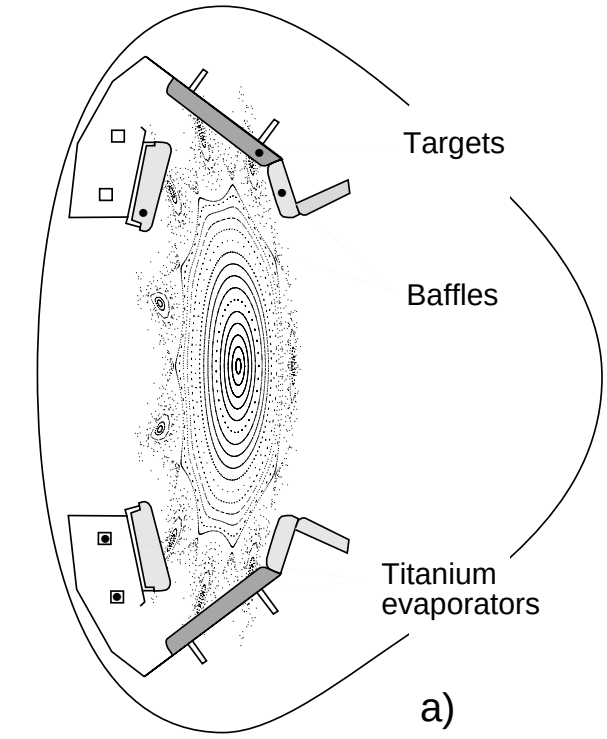

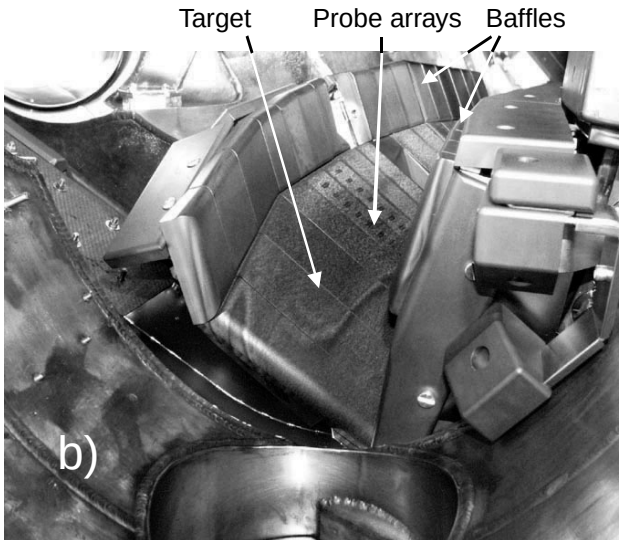

Fig. 1. (a) Elliptical plasma cross section with island divertor modules. Such modules are installed at the top and bottom of each of the five elliptical planes. The toroidal length of each module is 0.7 m. (b) Photograph of a bottom divertor module.

These features are completely changed in the UHD regime, as shown in Fig. 2. The energy confinement time τ_E increases steeply with density and then saturates. Provided that the plasma minor radius a is not significantly changed at finite beta, the values lie up to about a factor of two above the ISS95 scaling [4] at high density. Although the database of the ISS95 scaling includes neither such configurations nor such high densities, the reference serves to elucidate the tendencies. In contrast to τ_E, the particle and impurity confinement times decrease with increasing density. This also allows full density control and quasi-steady-state operation under conditions of partial detachment (see below) from the divertor targets. The degradation of τ_E in detached scenarios is moderate. With the exception of the lowest density cases, all data points in Fig. 2 were obtained from quasi-steady-state discharges. Typical electron temperatures (not shown) are 400–500 eV at the center and between about 20 eV (partially detached) and 100 eV (attached) near the separatrix. Radiated power fractions are low to moderate in attached regimes and reach up to about 90% in detachment scenarios. The radiation always stays peaked at the edge and originates from lower ionization states of carbon and oxygen. The density n_{es} near the separatrix first steeply increases with $\overline{n}_e$, saturates at $\overline{n}_e > 2 \times 10^{20}$ m^{-3}, and then drops more or less (depending on the external gas feed) in partially detached states. Neutral pressures in the divertor subvolumes increase with density and reach values near 10^{-3} mbar, which should be sufficient for the planned active particle pumping by titanium gettering. Partially detached discharges with strong external gas feed already exhibit a strong drop of n_{es}, increased radiation, and higher neutral pressure at lower density than discharges with weak gas fuelling.

Divertor plasma properties

The divertor regimes show — as should be expected for such a complex, three-dimensional scrape-off layer (SOL) and divertor structure — a rather multifarious picture. Here we describe the main features obtained with diagnostics concentrated at two opposite (top and bottom) divertor modules. Because of the island structure, the main interaction of the plasma with the targets typically concentrates at two helical stripes (from 2-D thermography and H_α cameras). An example (H_α traces) is shown in Fig. 3, which also defines the target tile and probe position nomenclature used below. The radially inner stripe splits into two closely neighboring peaks when approaching tile 12 (defined as watershed), which is closest to the main plasma. Within the strike zones, the thermal load shows strongest maxima at the watershed and at tiles further from the main plasma but with steeper inclination to the field lines (typically at tile 5 or 6). Concerning rollover and detachment of the energy and particle fluxes (see below), H_α, thermography and probe data indicate a rather uniform behavior over most of the target plate, with the exception of the "wing" zone (tiles 4–6), where the behavior is clearly different. In order to simplify further descriptions, in the following the wing region is designated as "region A" (attached) and the remaining area as "region D" (detached).

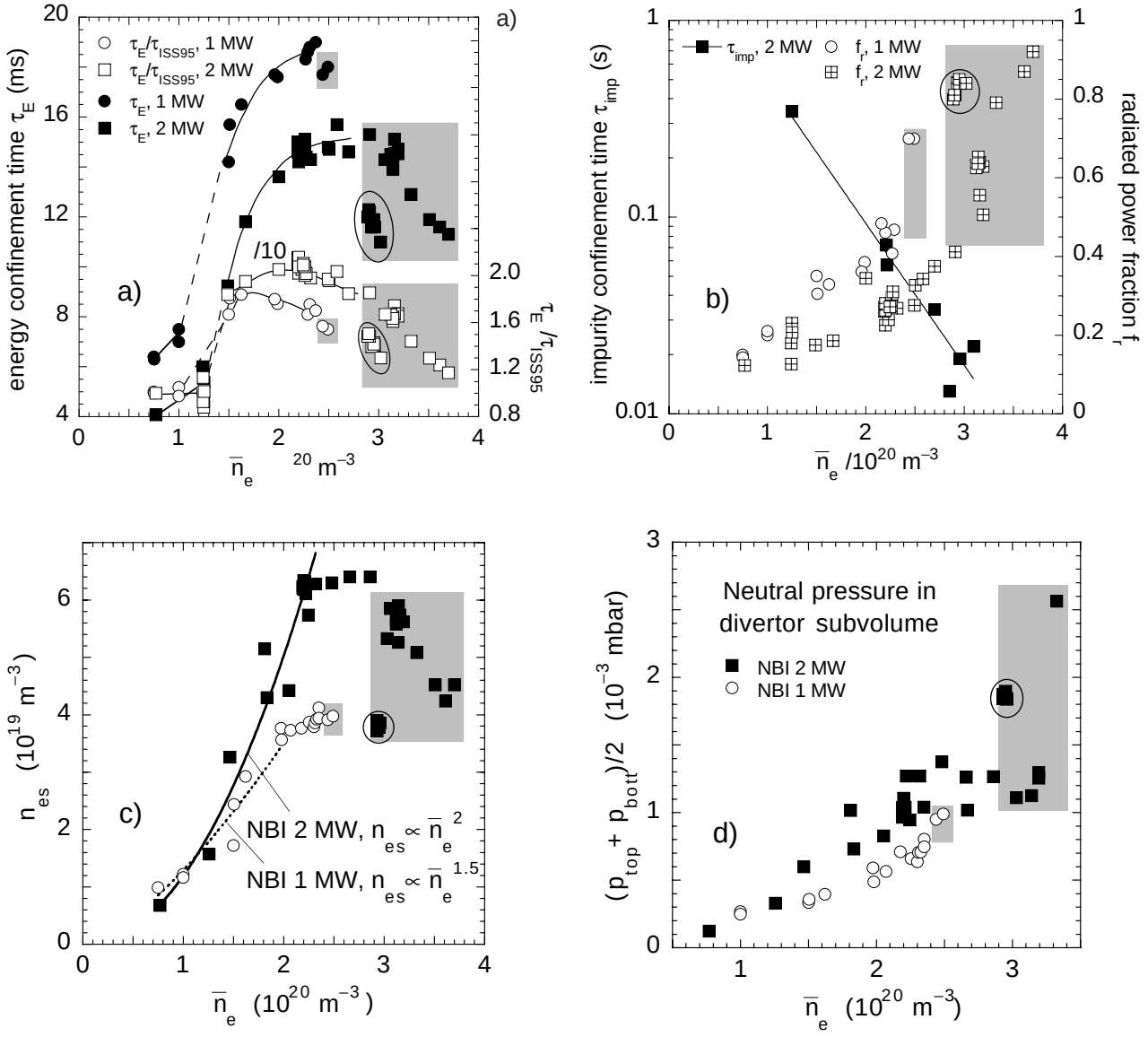

Fig. 2. Parameters as functions of the line-averaged density $\bar{n}_e$ for NBI-heated discharges. Shaded ranges indicate partial detachment from target region D (see Fig. 3). Encircled data points correspond to discharges with strong external gas feed. (a) Energy confinement times τ_E and ratios τ_E/τ_{ISS95} (see text). (b) Impurity confinement times τ_{imp} and radiated power fractions $f_r = P_{rad}/P_{NBI}^{abs}$. (c) Densities n_{es} at the upstream separatrix position (from lithium beam). (d) Neutral pressures measured in the divertor subvolume (average of top and bottom modules).

Figure 4 shows downstream peak densities n_{ed}^{peak} and corresponding temperatures T_{ed}^{peak} measured with probe arrays at tiles 13 (representative of region D) and 5 (region A) in quasi-steady-state discharges (NBI, 2 MW) are plotted versus $\bar{n}_e$ or n_{es}. The data indicate — in agreement with H_α and thermography data (not shown) — rollover and detachment of the particle and energy flux in region D with increasing density with no intermediate high-recycling regime. This latter characteristic was predicted by 3-D edge transport simulations (EMC3-EIRENE code [5, 6]) and is ascribed to frictional losses of parallel momentum due to cross-field particle transport in this specific geometry [7]. These losses, however, are insufficient to explain the onset of rollover at $T_{ed} > 10$ eV where charge-exchange losses cannot be responsible.

Both of these findings, the absence of high recycling scenarios and rollover at relatively high T_{ed} values, call into question whether the term "detachment" can be applied to the full range beyond the rollover point. Therefore, for the time being, the term is used here only for scenarios with extremely low particle flux and downstream temperatures close to or below the ionization threshold of hydrogen, as

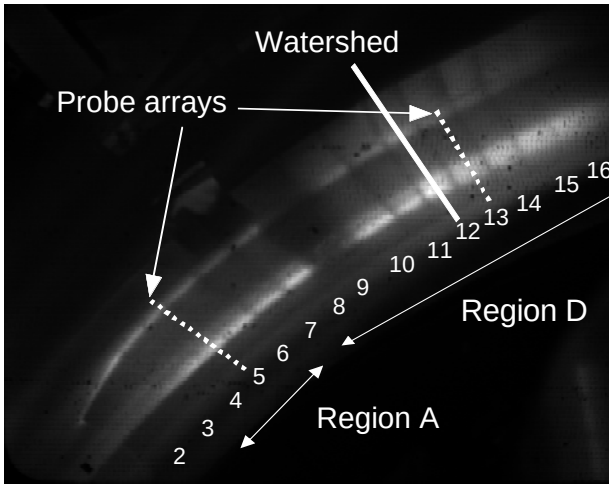

Fig. 3. View of a divertor target. H_α traces show that interaction with the plasma is concentrated at two helical stripes. The numbers denote target tiles for orientation. The watershed (tile 12) is closest to the main plasma. The separation from the main plasma increases with increasing toroidal distance from tile 12. Tile 9 is slightly retracted in order to allow diagnostic openings. Regions A and D show different features with respect to rollover and detachment.

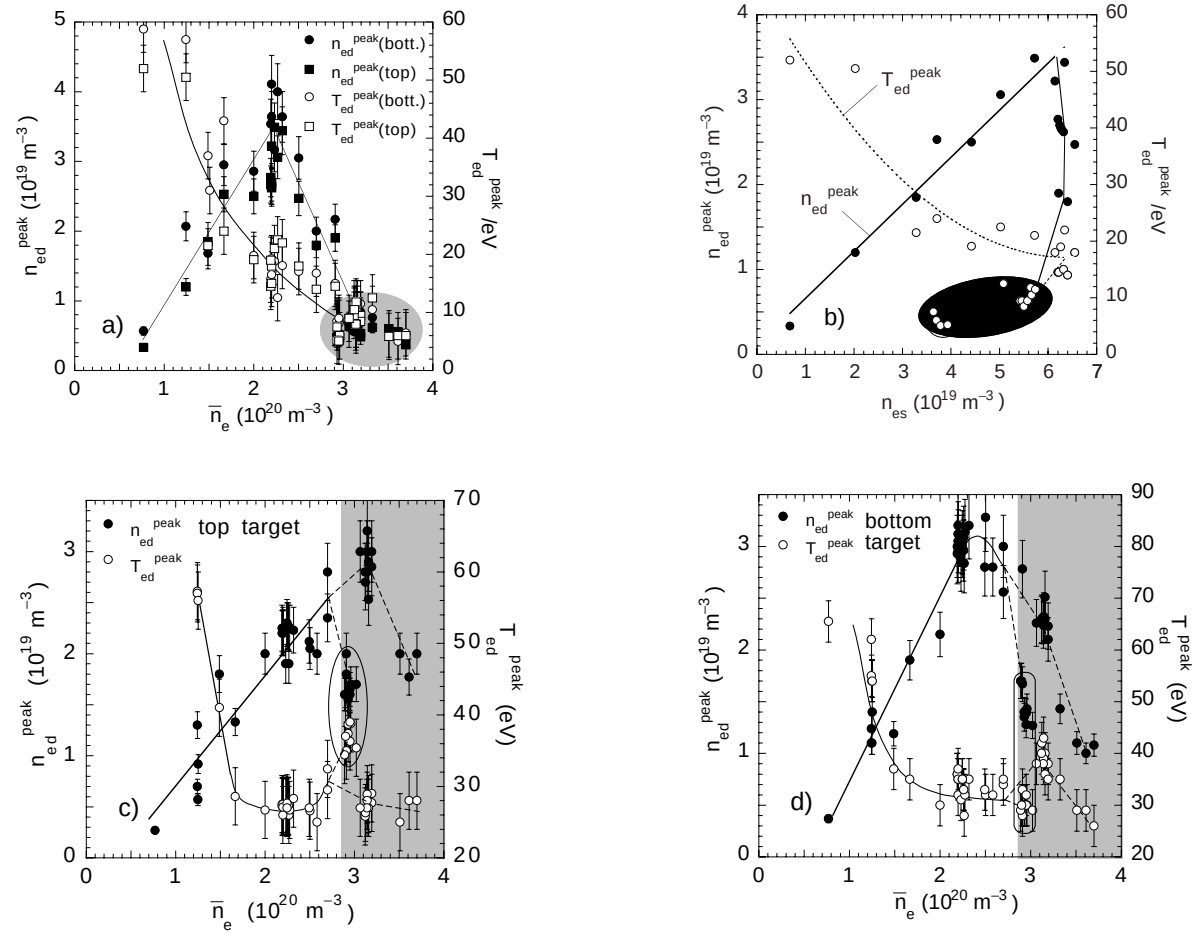

Figure 4. Peak downstream densities n_{ed}^{peak} and temperatures T_{ed}^{peak} measured with the probe arrays at (a) tile 13 (representative of target region D) and (b) tile 5 (representative of region A) for discharges with 2 MW of NBI**.** Shaded areas indicate detachment from region D. Encircled data points correspond to discharges with strong external gas feed. **(**a) Peak values at tile 13 (top and bottom) versus the line-averaged density $\bar{n}_e$. (b) Peak values at tile 13 (top) versus the upstream edge density n_{es}. Lines indicate the development towards detachment. (c)**,** (d) Peak values measured by the probe arrays at tile 5 (top and bottom, region A). They show a top/bottom asymmetry and indicate that the plasma stays attached at these positions.

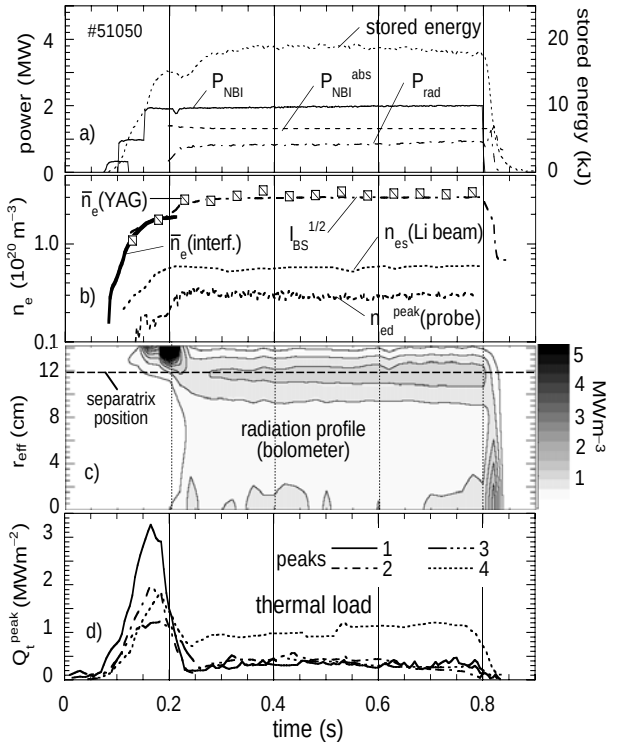

Fig. 5. A discharge with stable partial detachment. (a) NBI power P_{NBI}, absorbed NBI power P_{NBI}^{abs}, radiated power P_{rad}, and stored energy. (b) Line-averaged density $\bar{n}_e$ from microwave interferometer and YAG laser scattering, square root of the intensity of the bremsstrahlung $I_{BS}^{1/2}$ (calibrated by the interferometer data), density n_{es} near the separatrix, and maximum density n_{ed} near the target. (c) Abel-inverted radiation profile from 32-channel bolometer camera. (d) Peak power load from thermography on four target positions, indicated by the numbers 1–4. Three of them indicate detachment at about 0.2 s. At the fourth position (outer peak at tile 5, region A, see also Fig. 7), the plasma stays attached.

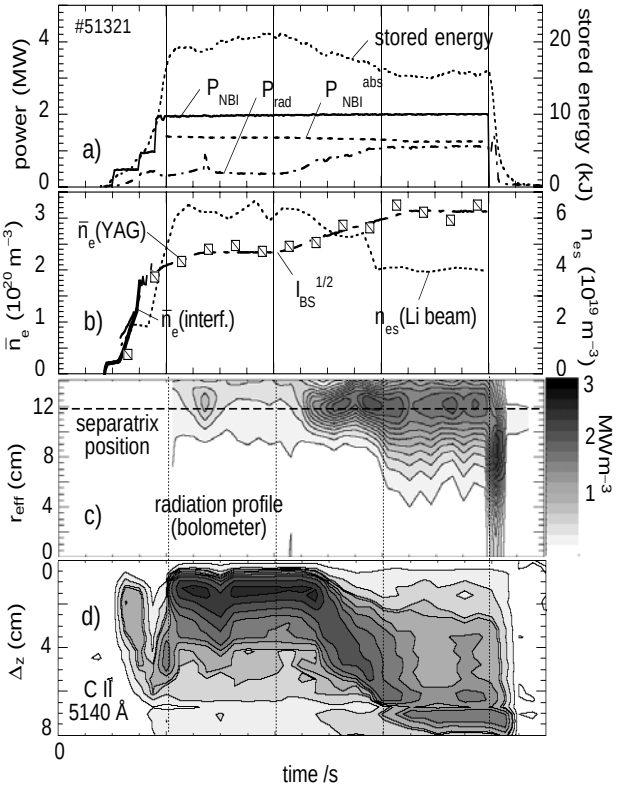

Fig. 6. A controlled transition to (strong) partial detachment; terms as in Fig. 5. The density is linearly ramped up from a lower level (attached) to a higher plateau (partially detached). The radiation stays peaked at the edge [Fig. 6(c)] but extends more towards the center compared with the discharge shown in Fig. 4. Figure 6(d) plots the radial spread Δ_z of the C II line radiation (5140 Å) relative to the target. The low-temperature front indicated by this peak continuously shifts from the target (position 0) towards the X-point, which is separated by 8 cm from the target at this poloidal plane (tile 9).

is indicated by gray shaded areas in the corresponding figures. Detachment from the strike zones is partial in the sense that the particle flux remains finite and T_{ed} stays above 2 eV (from H_α/H_γ line intensities, not shown); below this value, volume recombination becomes important.

A main result, however, is that the approach to this type of detachment is continuous. All intermediate states including partial detachment can be quasi-steadily maintained. One of the potentially stabilizing effects is that detachment is partial also in a spatial sense: the plasma in region A stays always attached at certain positions. Maximum temperatures T_{ed}^{peak} and densities n_{ed}^{peak} measured with probe arrays at tiles 5 [Figs. 4(c), 4(d)] indicate a complex interplay between top and bottom targets that changes with density and the strength of the external gas feed. But finally, the plasma stays locally attached in this region even at the highest density. During detachment from region D, the T_{ed}^{peak} values in region A exceed the upstream edge temperatures of about 20 eV measured by Thomson scattering at the high-field side of a triangular cross section, which points to an inhomogeneous temperature distribution near the separatrix.

An example for a discharge with stable, "weak" partial detachment is shown in Fig. 5. Since the density exceeds the operational range of the microwave interferometer (2 mm, second harmonic) in this type of discharge, it was controlled via the square root of the intensity I_{BS} of the bremsstrahlung. As the example shows, the $I_{BS}^{1/2}$ values (calibrated by the interferometer data in the lower density range) fit the data from the YAG laser scattering system well. The radiation is peaked at the separatrix position

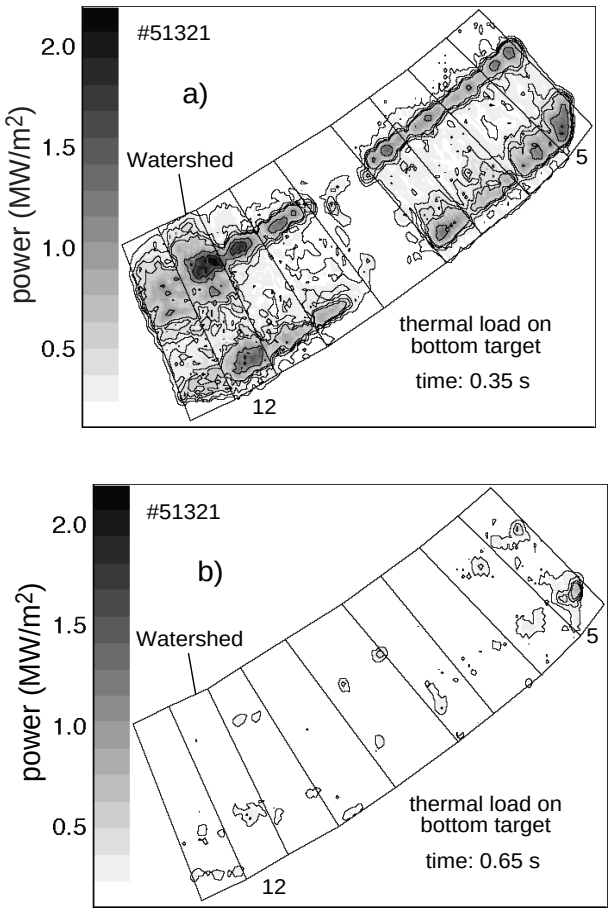

Fig. 7. Thermal load distributions on the bottom target from thermography (a) at 0.35 s (attached) and (b) at 0.65 s (partially detached) for the discharge shown in Fig. 6.

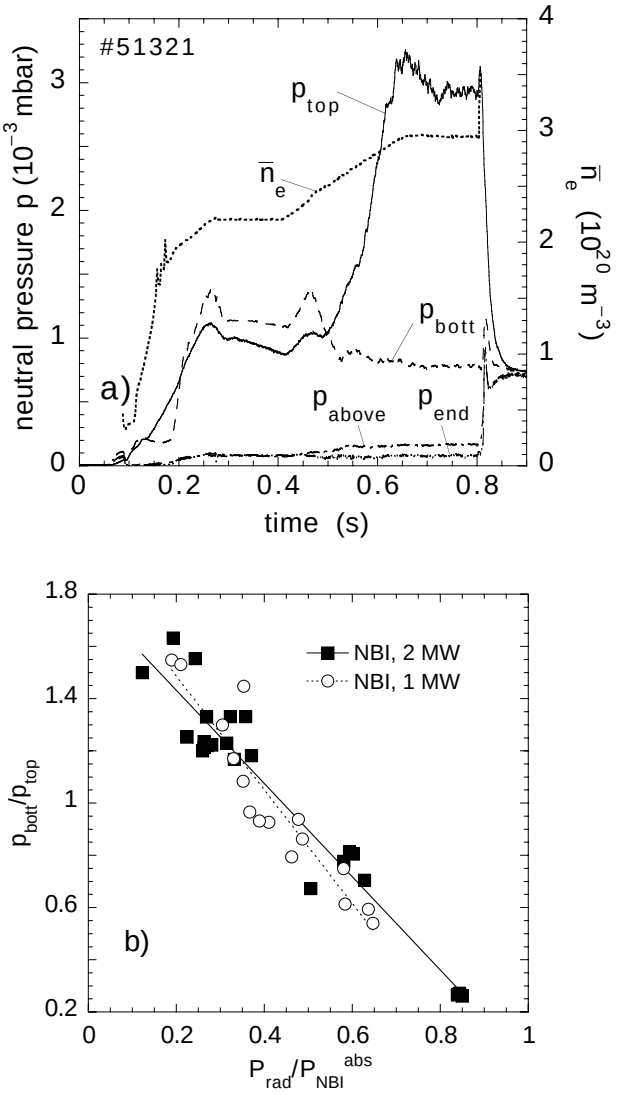

Fig. 8. (a) Neutral pressures p measured in the upper (p_{top}) and lower (p_{bott}) divertor subvolumes and in the main chamber beside (p_{end}) and above (p_{above}) the bottom divertor at the inner wall for the discharge shown in Fig. 6. (b) Ratio p_{bott}/p_{top} of the neutral pressures in the bottom and top divertor subvolumes versus the radiated power fraction P_{rad}/P_{NBI}^{abs} as an ordering parameter.

[Fig. 5(c)]. The radiated power fraction (not including radiation from the divertors) reaches about 70% in this case. Consequently, the peak thermal load on the target [Fig. 5(d)] is strongly reduced in the detached phase. Prior to detachment, the load shows four local maxima at the target, indicated by the numbers 1–4 in the figure. Three of them indicate detachment in agreement with H_α and probe data. At the fourth position (outer peak on tile 5 in region A) the plasma stays attached — in agreement with the H_α and probe data — as already mentioned above.

The transition from attached to partially detached states can be performed in a controlled way, as shown by an example in Fig. 6. In this case the line-averaged density $\bar{n}_e$ was linearly ramped from a lower level (attached) to a higher plateau (partially detached) by strong external gas feed. In the second plateau phase the $\bar{n}_e$ value does not exceed that of the discharge shown in Fig. 5. But, compared with that example, the stored energy [Fig. 6(a)] is reduced in this phase, and the upstream density n_{es} is decreased [Fig. 6(b)] as is typical for discharges with strong gas feed. The radiated power fraction is about 85% ("strong" detachment), but the radiation zone remains concentrated mainly at the edge [Fig. 6(c)].

As in the other examples, the radiation originates primarily from lower ionization states of carbon and oxygen. As already mentioned, the transition from the attached to the detached state is continuous, as demonstrated in Fig. 6d. The figure shows that the low-temperature front — indicated by the maximum of the C II (5140 Å) line radiation — and hence the ionization zone does not jump but contin-

uously moves with increasing density from the target towards the X-point radial position. The line intensity was measured by a spectrometer imaging the range between tile 9 (see Fig. 3) and the X-point, which means that this result is representative for region D in agreement with corresponding H_α and probe data (not shown). Power flux patterns on the bottom target (from thermography) plotted in Fig. 7 demonstrate again that the plasma stays attached in region A [Fig. 7(b), radially outer deposition peak], but the load level is reduced compared with the peak load in the attached state [Fig. 7(a)].

The neutral pressures in the divertor subvolume show a strong top/bottom asymmetry (Fig. 8, see also Ref. [8]). With the transition to detachment, the pressure in the top divertor chamber is strongly increased whereas the pressure in the bottom chamber decreases slightly [Fig. 8(a)]. This relation becomes inverted towards lower density. A clear correlation with the total particle flux onto the targets is not found at detachment. As Fig. 8(b indicates, the radiated power fraction can serve as an ordering parameter.

Summary and conclusions

W7-AS is being operated with open divertor modules in order to experimentally evaluate the island divertor concept for the first time. The new divertors provide access to a new operational range with NBI at very high density (up to $\overline{n}_e = 3.5 \times 10^{20}$ m^{-3}) with promising confinement properties. The energy confinement time steeply increases with density. In contrast, the particle and impurity confinement times decrease with increasing density. The physics background of these new features is not yet clear. It is assumed that access to the new regime is primarily enabled by the enlarged coverage of the plasma-wall interaction region by carbon tiles, which improves the recycling properties (enlarged interaction area for transient particle pumping) and screens the plasma more efficiently from unfavorable interaction with the vessel wall.

The new regime allows full density control and quasi-steady-state operation as well as stable partial detachment from the divertor targets. The approach to partial detachment is continuous. At a given heating power and with increasing upstream edge density, the energy and particle fluxes on the near-plasma part of the targets show rollover without passing through a high-recycling regime. The radiation always stays peaked at the edge. Radiated power fractions are low to moderate in attached regimes and reach up to about 90% in detachment scenarios. The neutral pressures in the divertor subvolumes increase with density up to values sufficient for future active particle control via titanium gettering in W7-AS. They show a strong top/bottom asymmetry, particularly in partially detached states.

P. Grigull for the W7-AS Team
Max-Planck-Institut für Plasmaphysik
D-85748 Garching, Germany

E-mail: grigull@ipp.mpg.de

References

[1] H. Renner et al., Nucl. Fusion **40** (2000) 1083–1093.

[2] P. Grigull et al., presented at 28th EPS Conference. on Controlled Fusion and Plasma Physics, Funchal, Madeira, 2001, to be published in Plasma Phys. Controlled Fusion.

[3] K. McCormick et al., Plasma Phys. Controlled Fusion **41** (1999) B285–B304.

[4] U. Stroth et al., Nucl. Fusion **36**, 8 (1996) 1063-1077.

[5] Y. Feng, F. Sardei, and J. Kisslinger, J. Nucl. Mater. **266**–**269** (1999) 812.

[6] D. Reiter, Technical Report Jül-1947, KFA Jülich, Germany, 1984.

[7] Y. Feng, J. Kisslinger, and F. Sardei, in Proc. 26th EPS Conf. on Controlled. Fusion and Plasma Physics, Maastricht 1999, Europhys. Conf. Abstracts **23J**, Topic B, 1465.

[8] K. McCormick et al., presented at 28th EPS Conference. on Controlled Fusion and Plasma Physics, Funchal, Madeira, 2001, to be published in Plasma Phys. Controlled Fusion.